Electronic Supplementary Material (ESI) for Nanoscale.

Electronic Supporting Information

Self-spinning Nanoparticle Laden Microdroplets for Sensing with Energy Harvesting

Mitradip Bhattacharjee,[a] Viswanath Pasumarthi,[b] Joydip Chaudhuri,[b] Amit Kumar Singh,[a] Harshal Nemade[ac] and Dipankar Bandyopadhyay[*ab]

[a] *Centre for Nanotechnology, Indian Institute of Technology Guwahati, India*

[b] *Department of Chemical Engineering, Indian Institute of Technology Guwahati, India*

[c] *Department of Electronics and Electrical Engineering, Indian Institute of Technology Guwahati, India*

*Author to whom correspondences should be addressed. Email: dipban@iitg.ernet.in

I. Characterisations of Nanoparticles:

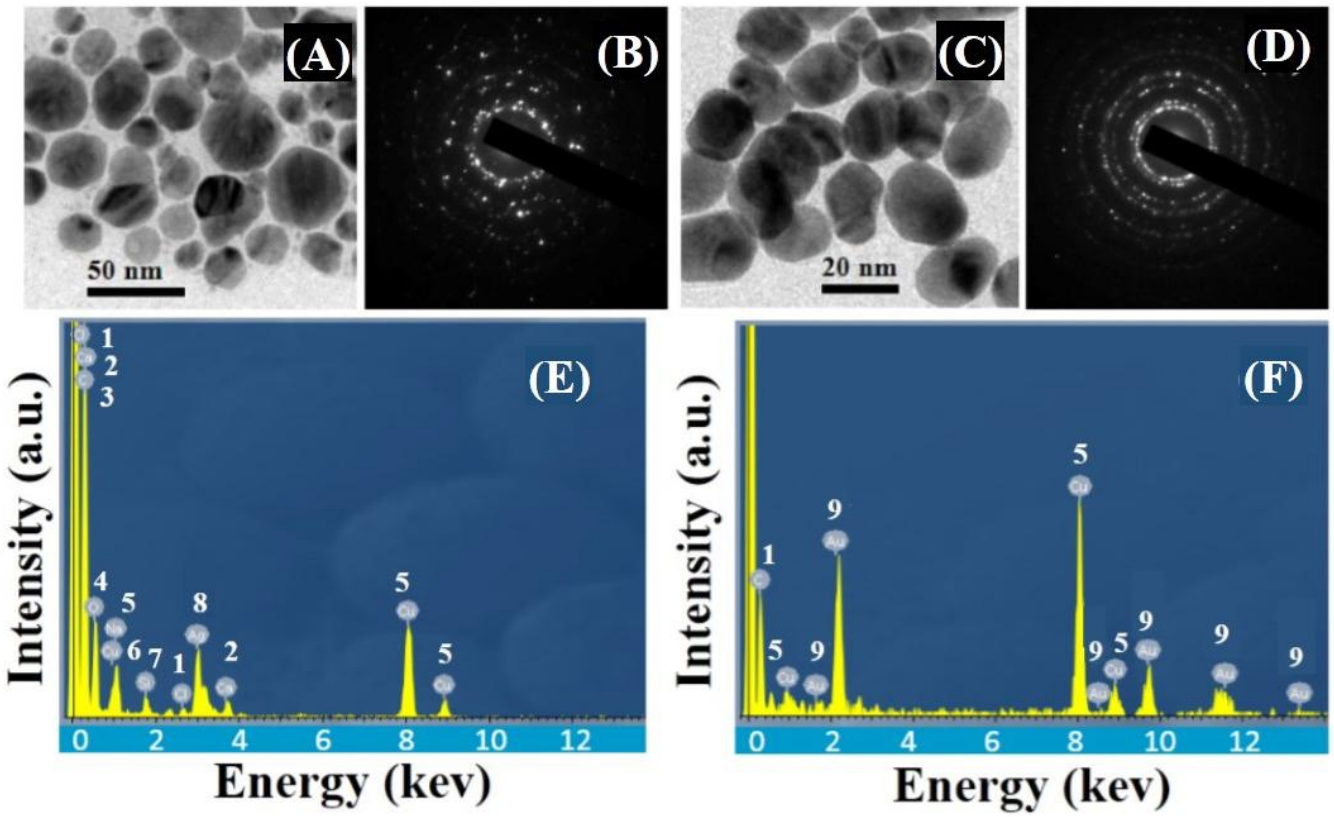

Figure S1. Characterisations of nanoparticles. Figures (A) and (C) are the TEM images of Ag and Au nanoparticles. Respective SAED patterns are shown in images (B) and (D). The EDX images (E) and (F) confirmed the presence of Ag and Au. The numbers 1 – 9 on the image (E) and (F) represent the peaks of Cl, Ca, C, O, Cu, Si, Ag, and Au, respectively.

Characterizations of Ag and Au nanoparticles have been shown in the **Figure S1**. Figs. S1A and S1C show the TEM images of Ag and Au nanoparticles with their respective SAED patterns in the images 1B and 1D. EDX analyses in the Figs. S1E and S1F confirmed the presence of Ag and Au in the sample. The images (A) and (E) show that the diameters of the Ag nanoparticles were about 10 nm to 50 nm whereas the Au nanoparticles were about 10 nm to 20 nm. The numbers 1 – 9 on the image (E) and (F) represent the peaks of Cl, Ca, C, O, Cu, Si, Ag, and Au, respectively.

II. Computational Simulations for the Rotational Motion:

A two-dimensional (2-D) semi-circular water droplet of diameter 1.5 mm, resting on a flat surface and surrounded by air was chosen to be the computational domain, as shown in the image (A) of **Figure S2**. The rectangular domain was of length 3 mm and width 1 mm. The droplet was placed at 0.75 mm

downstream from the air inlet. The surface tension gradient ($\Delta\gamma = \gamma_1 - \gamma_2$) at the interface was induced by changing the magnitude of surface tension at the arc length of 0.05 mm of the deformable air-water interface, as shown in the image (A) of **Figure S2.** The streamlines shown on the figure represent the rotational currents originating from the surface tension gradient at the air-water deformable interface. The arrows represent the local velocity vectors.

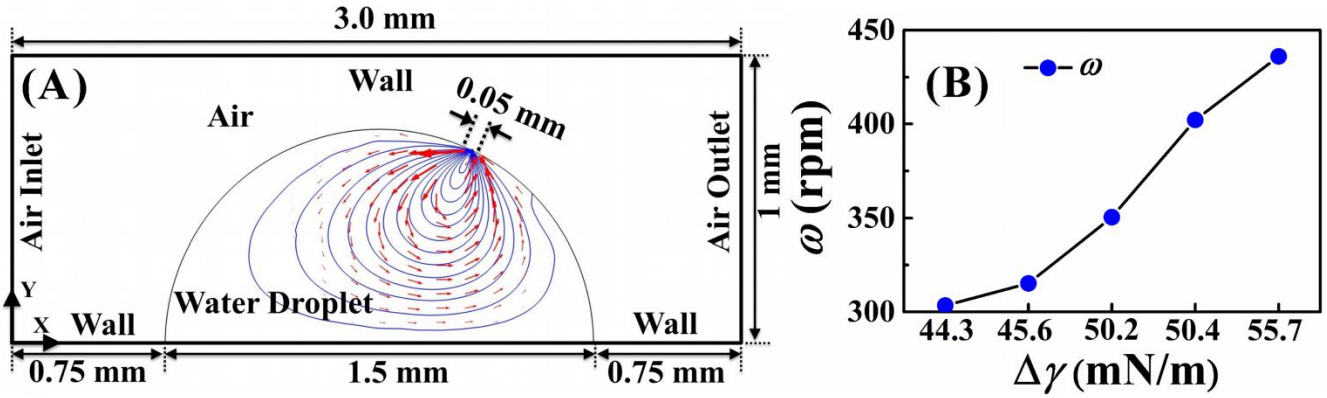

Figure S2. Results from simulations: Image (A) shows the streamlines and the velocity vectors for a droplet of diameter 1.5 mm. The surface tension at the air-water interface was set to 72.7 mN/m (γ_1) and changed locally to γ_2 at the 0.05 mm arc length as indicated the image. A surface tension gradient $\Delta\gamma = \gamma_1 - \gamma_2$ was created across the air-water interface. Image (B) shows the change in average angular velocity (ω) with change in surface tension gradient ($\Delta\gamma$) for different vapours sources such as toluene, chloroform, methanol, ethanol, and diethyl ether.[1]

In the computations, the air (gas) and water (liquid) phases were assumed to be immiscible, Newtonian, and incompressible. The following continuity and equations of motion were employed to describe the motion of the i^{th} phase,

$$\nabla \cdot \mathbf{u}_i = 0, \qquad (1)$$

$$\rho\left(\dot{\mathbf{u}}_i + \mathbf{u}_i \cdot \nabla \mathbf{u}_i\right) = \nabla \cdot \left[-p_i \mathbf{I} + \eta_i\left(\nabla \mathbf{u}_i + \nabla \mathbf{u}_i^{T}\right)\right] + \mathbf{f}_{st} + \rho \mathbf{g}. \qquad (2)$$

Here, the subscript i corresponds to air (i = 1) and water (i = 2) phases. The over-dot symbol denotes the time derivative. The velocity vector, density, viscosity, and pressure of the i^{th} phase were denoted by notations $\mathbf{u}_i$, ρ_i, η_i, and p_i respectively. The notation **g** was the acceleration due to gravity vector which was acting in the negative y-direction. The surface tension force was defined as, $\mathbf{f}_{st} = G\nabla\phi$, a product of the chemical potential (G) and the gradient of the phase field parameter (ϕ). The surface tension force

was determined by minimizing the total free energy inside fluid domain as a function of the phase field variable (ϕ),

$$F(\phi) = \int_{\Omega} \left(f(\phi) + \frac{1}{2}\lambda \left| \nabla^2 \phi \right| \right) d\Omega . \quad (3)$$

Where, Ω was computational volume and the total free energy, $F(\phi)$ was combination of double well potential, $f(\phi) = \lambda / 4N^2 \left(\phi^2 - 1\right)^2$, and surface energy. The parameter *N* was calculated by the following equation, $N = 0.5h_m$ where h_m is the maximum element size in the computational domain. To evaluate surface energy, mixing energy density (λ) was estimated as, $\lambda = \left(3\gamma N\right) / \left(2\sqrt{2}\right)$ in which γ was surface tension and *N* was the thickness of the diffused interface. In order to track the rotational Marangoni motion of the droplet at the air-water interface and in the bulk, the phase-field method was employed.[2-5] In this method, the transport equation was written in terms of the phase field parameter (ϕ) as,

$$\dot{\phi} + \mathbf{u}_i \cdot \nabla \phi = \nabla \cdot \chi \left(\nabla G \right) . \quad (4)$$

Where the chemical potential (*G*) was defined as a derivative of the free energy functional, $G = F'(\phi) = \lambda \left[-\nabla^2 \phi + \phi\left(\phi^2 - 1\right) / N^2 \right]$. The interfacial density (ρ), and viscosity (μ) were evaluated in terms of *f* as, $a = 0.5\left[a_1(1+\phi) + a_2(1-\phi)\right]$, where *a* can be any of ρ and μ. The symbol χ represents the mobility tuning parameter, which was chosen to be 10 m s/kg to avoid mass loss in the conventional phase field model. The lower flat surface of the droplet was assumed to be non-slipping and impermeable while the curved air-water interface was considered to be the deformable one. The velocity of air at the inlet and outlet were set to zero. The upper wall of the computational domain was assumed to be non-slipping and impermeable. The contact angle of water droplet on the substrate was considered to be 90°. The surface tension at the air-water interface was assumed to be constant at 72.7 mN/m (γ_1) and changed locally in the domain of 0.05 mm arc length to a smaller value (γ_2) to create the surface tension gradient ($\Delta\gamma = \gamma_1 - \gamma_2$), as shown in the image (A) of **Figure S2**.

The 2-D geometry was divided into 7642 triangular elements to obtain the grid independent solutions. The unsteady governing equations (1) – (4) together with the boundary conditions were solved using the commercially available COMSOL™ Multiphysics software based on the finite element method.[5] In this method, the spatial terms of the governing equations were initially discretized to obtain an ordinary differential equation (ODE) in time, which was time-marched to obtain the evolution of the streamline

flow patterns inside the droplet. We employed the built-in Galerkin least-square (GLS) method to discretize nonlinear convective diffusion equations, which was stabilized through streamlining and crosswind diffusions. Segregated predictor–corrector method had been used to obtain the velocity and pressure profiles by incremental pressure correction.

Image (B) in the **Figure S2** shows the variation in the average angular velocity (ω) with change in surface tension gradient ($\Delta\gamma$) for different vapours sources. The typical values of $\Delta\gamma$ were obtained for the computations from Ref. 1 as, toluene-water (44.3 mN/m), chloroform-water (45.6 mN/m), methanol-water (50.2 mN/m), ethanol-water (50.4 mN/m), and diethyl ether-water (55.7 mN/m). The plot clearly suggests that ω increased monotonically with $\Delta\gamma$. The simulations confirmed that indeed the magnitude of droplet rotations was a function of the $\Delta\gamma$ at the air-water interface.

III. Experimental Optimization of Salt and Nanoparticle Loading in the Droplet:

A. Characterization of the Electrolytes

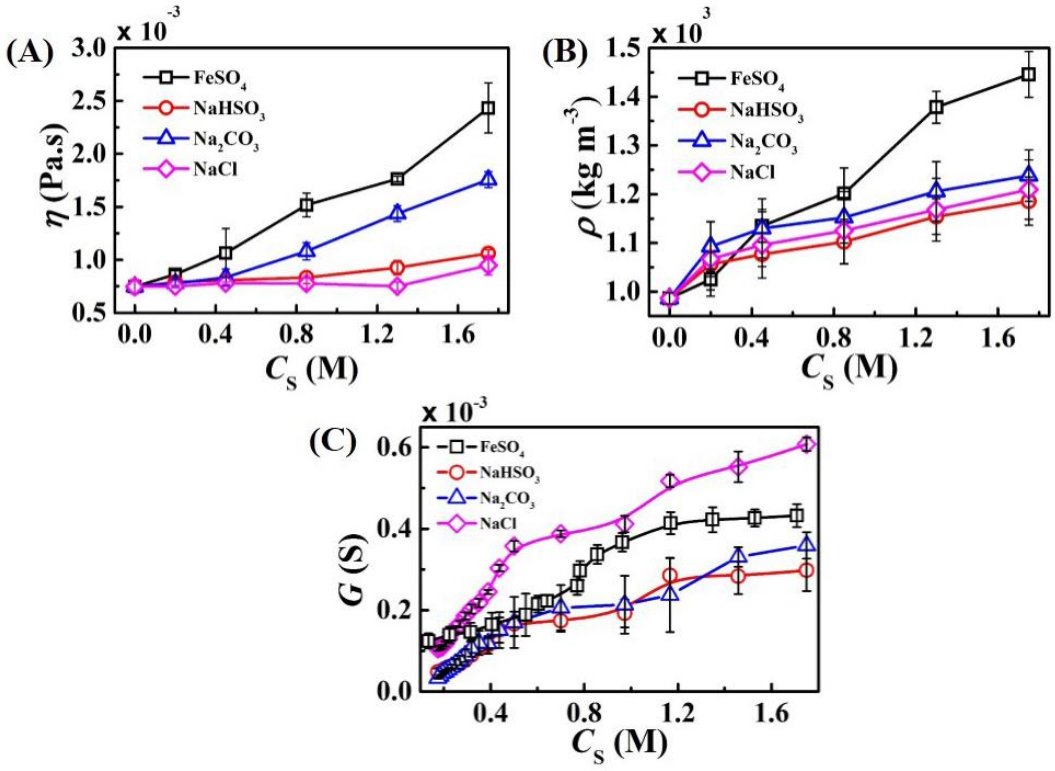

Figure S3: Characterization of electrolytes employed in the experiments. The plots show the variations in (A) viscosity, η, (B) density, ρ, and (C) electrical conductance G, of aqueous salt solutions of concentration (C_s) composed of four different salts $FeSO_4.7H_2O$, $NaHSO_4$, Na_2CO_3, and NaCl.

It is well known that deionized water is electrically non-conducting and addition of salt improves its electrical conductance significantly. Importantly, an increase in the salt-loading also increases the viscosity and density of a liquid. We employed four different types of salts, $FeSO_4.7H_2O$, $NaHSO_4$, Na_2CO_3, and NaCl, to identify the type of salt to be employed in the experiments. The plots (A) – (C) in **Figure S3** show the variations in viscosity (η), density (ρ), and electrical conductance (G) with the concentration of different salts (C_s) in water. The viscosities of the salt-water electrolyte were measured employing the interfacial rheometer (Anton Paar, Physica MCR301) following the ASTM Standard procedure D1331-11 (2001). The densities of the electrolytes were obtained by measuring the mass of 10 ml salt-water solutions in a high precision weighing machine with digital output (Metlar Toledo, ME204). The electrical resistance of the salt-water solutions was measured with the help of a digital multimeter (Mastech, India, range: 0 – 2 MΩ ± 1.0%) by placing a pair of cylindrical electrodes (diameter ~ 2 mm) into a solution of 20 ml electrolyte. The inverse of this resistance is reported as the electrical conductance (G) in the plot (C). The plots suggest that apart from the increase in the electrical conductance (G), the viscosity (η) and density (ρ) of the electrolytes increased with C_s. The plots also suggest that G values were significantly higher for the salts $FeSO_4.7H_2O$ and NaCl, which prompted us to choose the salt in between these two materials.

B. Optimization of Salt and Nanoparticle Loading in the Rotating Droplets:

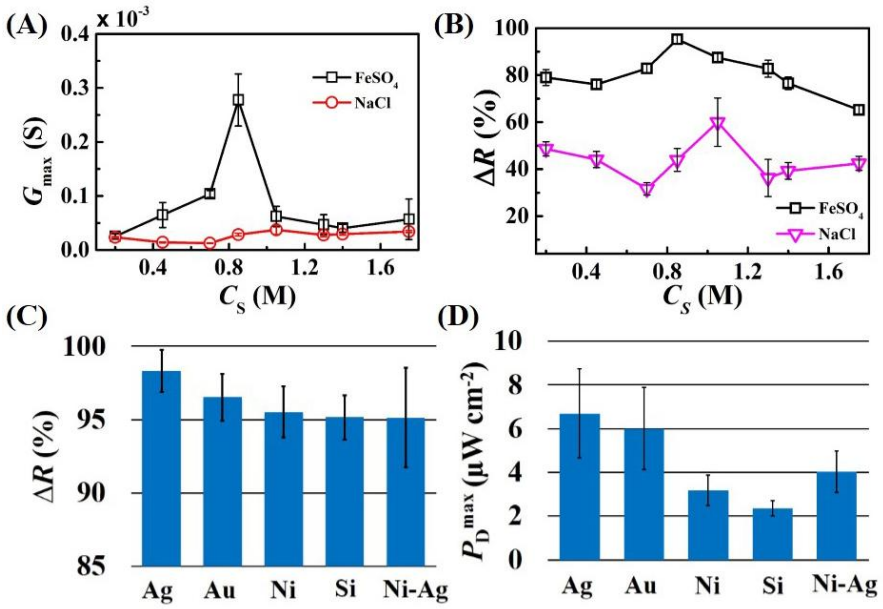

Figure S4: The plots show the variations in the, (A) electrical conductance (G_{max}) when the droplet was rotating at its maximum speed under organic vapour excitation and (B) percentage change in resistance

in such a situation, $\Delta R = 100 \times \left(R_0 - R_{\min} \right) / R_0$, with the concentration of salt (C_s). Plots (C) and (D) show the variations in ΔR and maximum power density ($P_D^{\max}$) across the droplet of aqueous 0.85M $Fe_2SO_4.7H_2O$ suspended with different types of nanoparticles. In all the experiments, the nanoparticles and the aqueous salt solution were mixed in 1:1 (v/v) ratio.

We also carried out a series of experiments with rotating droplets to optimize the salt concentration and the nanoparticle loading inside the droplet. Images (A) and (B) in **Figure S4** show that the variations in the electrical conductance ($G_{\max}$) when the droplets were rotating at the maximum speed under the organic vapour excitation and the corresponding percentage variation in resistance ($\Delta R = 100 \times \left(1 - R_N^{\min} \right)$) with the change in C_s. In this study, R_0 is the experimentally measured electrical resistance of the stationary droplet, $R_{\min}$ is the minimum resistance measured for a rotating droplet when its speed is at maximum, and $R_N^{\min}$ (= $R_{\min}/R_0$) is the ratio of the previous two parameters. In these experiments, the electrical resistance was measured with the help of a digital multimeter (Mastech, India, range: 0 – 2 MΩ ± 1.0%) by placing a pair of cylindrical electrodes (diameter ~170 μm) into a microdroplet of diameter ~2 mm. Plot (B) suggests that the electrical resistance of the stationary droplet (R_0) had been always higher than the rotating one, and it reached a minimum value ($R_{\min}$) when the droplet reached the maximum rotational speed under the organic vapour excitation. The plots (A) and (B) suggest that the variations in $G_{\max}$ and ΔR were rather non-monotonic with increase in the C_s when the salts were NaCl and $FeSO_4.7H_2O$. We observed that with an increase in C_s, ΔR and $G_{\max}$ for the rotating droplets increased to a maximum value before reducing sharply at very high salt-loading. The sharp reduction at higher C_s could be attributed to the weakening of the rotational motion beyond a threshold salt-loading due to the increase in viscosity and density of the droplet. The experiments suggested that among all the salts tested at various concentrations, a water droplet loaded with 0.85M $FeSO_4.7H_2O$ showed maximum variation in ΔR when the microdroplet rotated at a maximum speed under the organic vapour stimulation. Thus, the aqueous solution of 0.85M $FeSO_4.7H_2O$ was chosen to be the system for study.

In order to understand the impact of suspended nanoparticles on the droplet motion and their influence on the electrical properties of the droplet, we tested with different types of nanoparticles, for example, Ag, Au, Ni, Si, and Ni-Ag core shell. The nanoparticles were introduced because of three reasons, (i) they were insoluble and non-reactive to water, (ii) presence of nanoparticles helped in retaining the point of minimum resistance ($R_{\min}$) for a longer duration, and (iii) the energy and power generation was higher

in presence of the suspended nanoparticles because of the increase in the electrical conductance of the droplet. Plots (C) and (D) in the **Figure S4** show the variation in ΔR and maximum power density (P_D^{max}) for different nanoparticles when suspended in the salt-water droplet in a 1:1 (v/v) ratio. The plots clearly suggest that the power density obtained was higher for the Ag and Au nanoparticles than the other nanoparticles and this was the basis to employ the Ag and Au nanoparticles in the experiments reported in the main manuscript. The suspended Ag and Au inside the droplet enhanced the electrical conductance of the salt-water droplet, which eventually helped in lowering the resistance while it rotated under the organic vapour excitation.[1]

IV. Computational Simulations to Estimate Potential Drop on the Electrodes:

Figure 3 in the manuscript shows the experimental setup for energy harvesting. In the beginning of the experiment, a salt-water droplet was placed on a pair of Cu electrodes and the vapour source was introduced near the air-water interface to induce the rotational motion inside the droplet. The **supporting video 3** shows the cycle of different events on the droplet motion and the subsequent variation in the resistance across the droplet (R) with time (t). The entire event could be divided into three stages: (i) initially, the resistance of the stationary droplet was measured to be R_0; (ii) following this, the introduction of the vapour source triggered the rotational motion and with time R progressively reduced to a minimum value of R_{min}; (iii) finally, after the withdrawal of the vapour excitation when the droplet became stationary, R increased near to the base value R_0. In this situation, the change in the electrical resistance was measured with a multimeter. Importantly, with the same system, we obtained a potential difference across the electrodes while the droplet was undergoing the rotational motion and a nanovoltmeter was connected to the electrical circuit replacing the multimeter. It is well known that when a Cu electrode is immersed in water, a negative ζ-potential (– 29 mV) is generated due to the formation of an electrical double layer (EDL).[6] Further, in such a situation, it is also well known that the thickness of the EDL can shrink and become non-existent upon salt loading in the water. Thus, a stationary salt-water droplet is expected to show zero potential difference across the Cu electrodes, which we observed in the experiments. However, when the vapour source was introduced near one of the electrodes, the rotational motion inside the droplet could dislodge a part of the salt ions from the EDL to partially restore the negative ζ-potential. Importantly, since the vapour source stimulation was towards one of the sides of the droplet, a

stronger rotational motion near one of the electrodes ensured that the salt particles dislodged asymmetrically from the EDLs near the Cu electrodes to create the potential difference between them.

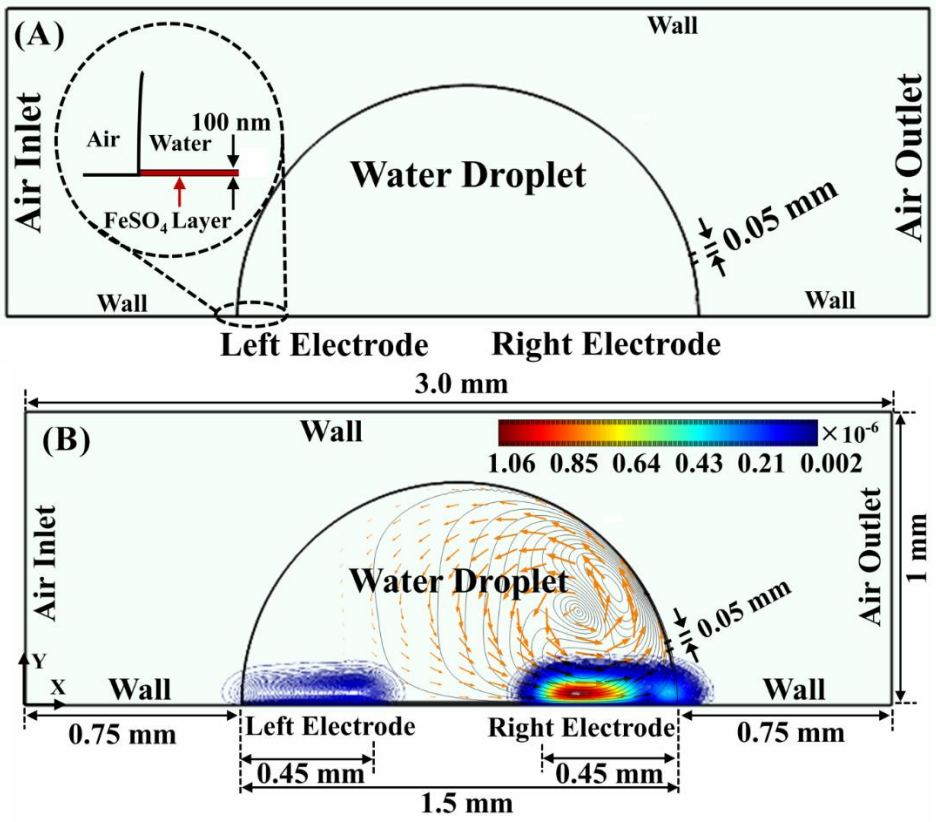

Figure S5. Image (A) shows the initial configuration of the computational domain at time 0 s, with 100 nm thick $FeSO_4$ deposited over the electrodes inside a water droplet of diameter 1.5 mm. Image (B) shows the streamlines (continuous lines), velocity vectors (orange arrows) for the bulk fluid motion and the coloured contour plot of convective flux magnitude, which was created due to the solutal Marangoni motion at the surface of droplet generated by sharp gradient of interfacial tension after 0.01 s of diethyl ether vapour exposure. The surface tension at the air-water interface was set to 72.7 mN/m (γ_1) and changed locally to the value of diethyl ether, 17.0 mN/m (γ_2), at the arc of length 0.05 mm. A surface tension gradient of $\Delta\gamma$ = 55.7 mN/m was created across the air-water interface to mimic the diethyl ether- water system as employed in the experiments.[1]

In **Figure S5,** we show a simple qualitative computational analysis, which justifies the onset of the potential difference across the electrodes during the droplet rotation. It may be noted here that we employed the same 2-D geometry as shown in **Figure S2**, with a simple modification near the base of the droplet where electrodes of length 0.45 mm was introduced, mimicking the experimental setup.

Further, in addition to the governing equations (1) – (4) shown in the section II, we solved the following convection-diffusion equation for the salt-water droplet,

$$\frac{\partial C_s}{\partial t} + \nabla \cdot \left(-D\nabla C_s \right) + \mathbf{u_2} \cdot \nabla C_s = \mathbf{0}. \qquad (5)$$

Here the concentration and diffusivity of salt in water are denoted by C_s and D whose values were taken to be, 0.85 M and 10^{-12} m^2/s, respectively, inside the droplet. It may be noted here that the diffusion coefficient was chosen to be very small in order to restrict any diffusion of salt from the electrodes. The conditions set in the simulations ensured that the salt molecules stayed near the electrodes until or unless a very strong convective current dislodged them from the electrode premises. The 2-D geometry was divided into 127653 triangular elements not only to obtain the grid independent solutions but also to resolve the EDL near the electrode for an aqueous salt solution of 0.85 M. The refined grid placing ensured that the first layer of the cells was of the thickness similar to the EDL for a salt-water droplet. The boundary conditions and the computational methodology employed for this analysis remained similar to the one discussed previously in the section II. It may be noted here that the lower wall was assumed to be impermeable for any salt diffusion to take place.

Image (A) in the **Figure S5** shows the initial configuration of the computational domain where the rectangular areas of height 100 nm above the electrode regions were assumed to have higher concentration of the salt while in the other parts of the droplet the salt concentration was 0.85 M. Image (B) in the **Figure S5** shows the streamlines and velocity vectors after 0.01 s, once the rotational motion was set inside the droplet. Image (B) in the **Figure S5** also shows the magnitude of the convective flux ($\mathbf{N}_{i,conv} = C_s \mathbf{u_2}$) near the electrodes inside the droplet after 0.01 s of diethyl ether vapour exposure. Clearly, the image (B) suggests that the rotational motion inside the droplet created an asymmetric convective flux near the electrodes, which in turn led to the difference in the concentration of salt near the Cu electrodes. The convective flux on the right side of the droplet was found to be ~10^3 times stronger than the same on the left side of the droplet. The simulations suggested that the right-heavy rotational motion was capable of dislodging significant amount of counter ions from the EDLs to the bulk of water droplet.

V. Supplementary Videos:

Supporting video S1 shows the main phenomenon behind this study. The video depicts the rotational currents on the surface and in the bulk of a water droplet when exposed to the vapour of diethyl ether. The droplet was deliberately loaded with a collection of inert iron/iron oxide microparticles to show the strength of the rotational current. The diethyl ether vapour was exposed in the immediate vicinity of the droplet surface to engender the motion. The video corresponds to the results and discussions shown with the Figure 1 of the main manuscript.

Supporting video S2 shows the strong rotational currents when a water microdroplet loaded with a collection of iron microparticles and a capillary tube filled with diethyl ether was brought near the surface of the droplet. The video corresponds to the results and discussions shown in the Figure 1 of the main manuscript.

Supporting video S3 demonstrates a typical cycle of change in resistance *R* with respect to the time when the diethyl ether vapour was introduced near the ionic droplet of 0.85M $FeSO_4$, $7H_2O$. The measurement was taken using a digital multimeter. The variations in the multimeter reading suggest a reduction (increase) in the electrical resistance (conductance) with the introduction of the organic vapour in the 'pulse' mode. The video corresponds to the results and discussions shown in the Figure 3 of the main manuscript.

Supporting Video S4 demonstrates the generation of voltage across, (1) a DI water droplet, (2) a single salt-water droplet loaded with suspended Ag nanoparticles, (3) two salt-water droplets loaded with suspended Ag nanoparticles, and (4) three salt-water droplets loaded with suspended Ag nanoparticles. In order to generate the voltage, diethyl ether vapour was introduced near the surface of the droplet(s). The nanovoltmeter readings in the video clearly show the increase in voltage as we increased the number of droplets connected in series, as schematically shown in the Figure 9 of the main manuscript.

Supporting video S5 demonstrates that the LED was off when the droplet was stationary. Thereafter, when the diethyl ether source was introduced the LED was turned on to indicate the presence of the vapour. Introduction of vapour decreased the resistance across the droplet, which helped the LED to

glow, whereas removal of vapour source increased the droplet resistance to turn off the LED. The video corresponds to the results and discussions shown in the Figure 10 of the main manuscript.

References:

[1] J. A. Dean, *Lange's Handbook of Chemistry*, McGraw- Hill. Inc., New York, 15th Edn., 1999.

[2] M. Plapp, *Philos. Mag.* 2011, ***91***, 25-44.

[3] I. Steinbach, L. Zhang and M. Plapp, *Acta Mater.* 2012, ***60***, 2689-2701.

[4] P. Yue, C. Zhou, J. J. Feng, C. F. Ollivier-Gooch and H. H. Hu, *J. Comp. Phy.* 2006, ***219***, 47-67.

[5] COMSOL Multiphysics, *COMSOL Multiphysics Modeling Guide: Version 4.2a* 2011, COMSOL AB.

[6] A. Manikandan and M. Sathiyabama, *J. Nanomed. Nanotechnol.*, 2015, **6**, 1000251:1-5.